

Latest Edition

Welcome to the June 2012 edition of the TCAD News, which is mainly focusing on the many enhancements included in the G-2012.06 release of Sentaurus.

In the first half of 2012, we have witnessed growing momentum in the development of FinFET technology and high voltage SiC and GaN power devices. While key industry leaders have been supporting their leading edge device development efforts with Sentaurus 3D simulation, we continue to enhance Sentaurus with models for new materials, new transport phenomena, and even new switching mechanisms. The G-2012.06 release provides a number of enhancements in FinFET modeling addressing the 14nm node, and it helps prepare our customers for the challenges of scaling to 10nm with alternative channels and beyond. The first release of 3D Device Monte Carlo allows customers to use this alternative statistical approach for modeling FinFET devices with Si and p-SiGe channel material. To account for device variability, customers have been applying the computationally efficient and accurate impedance field method (IFM) for single devices and small cells with multiple transistors (e.g. SRAM). This release extends IFM capabilities to metal grain variability and geometry fluctuations. On the More Than Moore front, new capabilities support the development of SiC and GaN power devices, CMOS image sensors and photovoltaic devices. For device reliability and parasitic analysis, enhancements in Sentaurus Interconnect allow customers to analyze the parasitic effects in middle-of-line for FinFET devices, and new models address stress-related concerns such as crack propagation.

This release also introduces Sentaurus Visual, a state-of-the art visualization tool which combines improved ease of use and flexibility.

I trust you will enjoy reading this issue of TCAD News and, as always, I look forward to your feedback on topics you would like to see covered in future issues.

With warm regards,

Terry Ma
Vice President of Engineering, TCAD

Contact TCAD

For further information and inquiries:
tcad_team@synopsys.com

TCAD news

Sentaurus G-2012.06 Release

Sentaurus Process

Monte Carlo implant conformal doping

Conformal doping is one of the important characteristics of plasma implantation. In spite of the current incomplete understanding of the exact mechanisms underlying conformal doping in plasma implantation, owing in part to the many-body long-range interactions in the plasma, the following mechanisms are known to play a key role:

- ▶ The ions become ionized anywhere in the ambient and start their acceleration towards the silicon surface,
- ▶ The incident ions are scattered off other particles in the plasma/ambient and change their directions.

To account for such effects, an empirical model that is compatible with the standard implantation has been implemented in the G-2012.06 release. In this model, instead of launching all ions from above the device, as in standard implantation, some fraction of ions are launched along the device surface, that is, along the solid–ambient interface. The fraction of the ions launching from the surface can be specified by using `conformity` parameter in the implant command. If `conformity=0`, standard implant results will be obtained, and if `conformity=1`, fully conformal doping will be achieved.

Figure 1 shows the comparison between standard implant and conformal doping implants. In the figure on the right, with `conformity=1`, fully conformal doping is achieved in the trench. It is interesting to note that MC implant captures the subtle profile difference between the vertical and horizontal directions due to crystallographic differences in the simulation plane.

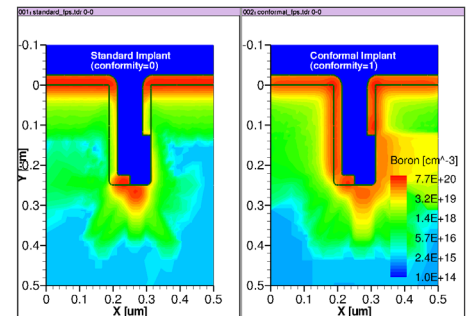


Figure 1: Implantation into a trench using (left) standard implantation mode and (right) conformal doping implant mode.

Enhancements to etching and deposition with the level set feature

The full level set initial value problem is a very general solution approach to etching and deposition, allowing single and multi-material operations, the inclusion of beam angle and shadowing effects, and the generalized definition of etching and deposition rates. The Lax-Friedrichs formulation provides additional stability and smoothness.

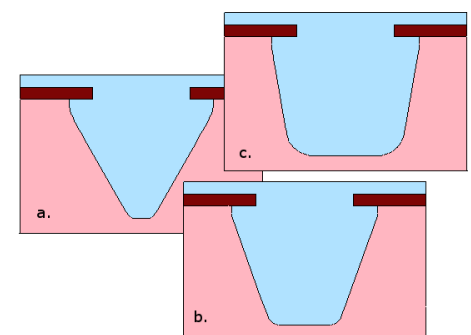


Figure 2: Full levelset trapezoidal etching with angle parameters: (a) 60, (b) 70, (c) 80. The other parameters are time=0.75, ambient.rate=0.3, roundness=1.



The full level set method with the Lax-Friedrichs formulation can now be explicitly chosen for additional structure modification in 2D and 3D. The `deposit` command now accepts the keyword `force.full.levelset`. Also, trapezoidal etching has been implemented using `force.full.levelset`.

Additionally, the `force.full.levelset` keyword can be used in the `mgoals` command to control the usage of the level set method in all instances of `etch` or `deposit` commands in the simulation. The keywords `force.full.levelset.etch` and `force.full.levelset.deposit` can be used to choose the level set method in `etch` and `deposit` commands, respectively.

The `angles.rates` etching type, also known as Piecewise-Linear etching rates, has been implemented using full level set, allowing general user definition of the etching rate as a function of the angle of the surface with the etching beam.

Improvements to speed of the mechanics solvers

The stress iterative solvers `sts2` (2D) and `sts3` (3D) are used in mechanics simulations. Several algorithmic changes were implemented in order to improve the performance of these solvers:

- ▶ A new scheme that takes into consideration results from previous linear system solutions was developed
- ▶ A dual residual minimization procedure which tracks the best local residuals and helps improve global convergence was developed for stress iterations

With these algorithmic improvements the speed of the stress solvers is improved by up to 33%, both in serial and parallel modes, as shown in table 1.

| Number of Threads | Elapsed time (s) F-2011.09 | Elapsed time (s) G-2012.06 | Speed up |
|-------------------|----------------------------|----------------------------|----------|
| 1 | 68,649 | 56,918 | 1.21x |
| 4 | 22,929 | 17,039 | 1.34x |
| 8 | 13,361 | 10,252 | 1.31x |
| 16 | 8,491 | 6,587 | 1.29x |

Table 1: Performance data based on the simulation of a rapid thermal processing (RTP) step for a 6T SRAM, with 1M grid points.

Progress in 3D oxidation

A new 3D oxidation algorithm named MovingMesh has been implemented in Sentaurus Process. Stability improvements over previous algorithms have been achieved through dynamic boundary repair and global mesh updating while preserving the accuracy of dopant profiles and geometric evolution. By maintaining a boundary representation (`b_rep`) and tetrahedral meshes, MovingMesh is able to ensure a high quality boundary while relying on standard mesh movement schemes which have been perfected over the years in 2D oxidation. This combination allows MovingMesh to ensure proper and accurate segregation as well as dopant dose conservation.

Over the course of an oxidation or other moving boundary step, the `b_rep` geometry is automatically smoothed when necessary by a new multi-material level set algorithm, followed by a new surface meshing algorithm. The combination of these new algorithms improves the stability and robustness of the simulation.

Figure 3 shows three 3D oxidation examples. The first example shows a vertical pillar structure [1]. The SiO_2 layer at the base corner has expanded 15 times from the initial 3nm to 45nm. The plot shows an oxidant concentration that is lower in the middle of the structure due to insulation by the silicon nitride. The lower end of silicon nitride was mechanically deformed by the expanded SiO_2 . It took 16 hours of CPU time to simulate 180 minutes oxidation.

The second example shows a local oxide of silicon (LOCOS) simulation of a power device structure. Initially we deposited the SiO_2 layer 0.015um uniformly. After 420 minutes of oxidation, the minimum and maximum SiO_2 thicknesses became 0.07um and 0.58um, respectively. The simulation took 38 hours with about 50,000 mesh points.

The last example shows a MOS transistor after a poly reoxidation step, which is the last step of the four oxidation steps in the process flow. The CPU time for the four steps of STI oxidation, sacrificial oxidation, gate oxidation, and poly reoxidation are 16 hours, 17 hours, 2 hours, and 3 hours respectively.

While we have found significant improvements in stability with MovingMesh over previous algorithms, further development is planned to make 3D oxidation a production quality feature, with a focus on improving runtime and resolution in thin layers.

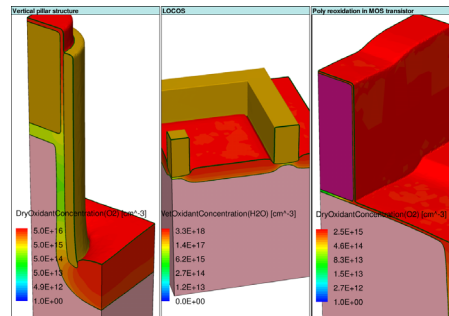


Figure 3: Three examples of 3D oxidation: vertical pillar structure, LOCOS, and poly reoxidation.



Sentaurus Process Kinetic Monte Carlo

Defect generation during solid phase epitaxy regrowth (SPER)

Amorphization of the silicon lattice by heavy ion implantation and subsequent recrystallization by solid phase epitaxial regrowth (SPER) is still a process widely used for silicon device processing. In particular, FinFET source and drain regions are subjected to amorphization and SPER during dopant implant and the subsequent annealing for activation. Planar MOSFETs are also typically manufactured with processes that include amorphization and subsequent SPER of the source and drain.

Experimental observations have shown that these processes typically lead to defective edges in the neighborhood of oxide filled trenches [2] and rectangular amorphized areas. The proximity of oxide interfaces retards the SPER and can produce twin boundary defects, and in some cases even leads to polysilicon formation.

Sentaurus Process KMC includes now a predictive model for defect formation during SPER, based on [3]. This model is an extension of the existing lattice kinetic Monte Carlo (LKMC) model which is used in the SPER simulation.

The model tracks the silicon lattice and detects three local distinct configurations in it. These microscopic configurations are called {100}, {110} and {111} because they are related with these macroscopic planes. This relation is, however, only qualitative. For instance, recrystallization in a {110} macroscopic plane involves both {110} and {100} microscopic events.

The {100}, {110} and {111} planes are defined according to the number of atoms they need so that each of them can bond to the crystalline phase with two undistorted bonds. Only 1 atom is needed for {100} local configurations, 2 for {110} and 3 for {111} [4].

This can be seen in Figure 4 which shows a projection of the Si lattice with facets in the named planes and the microscopic configurations needed to continue the regrowth.

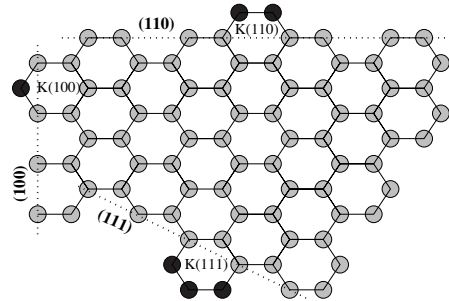


Figure 4: {100}, {110} and {111} microscopic configurations need 1, 2, and 3 atoms, respectively, to get two undistorted bonds.

The modeling of defect formation is done by assigning a “tag” to every crystalline atom. This tag has only two values: defective and non-defective. Non-defective atoms follow the original lattice orientation. Defective atoms are silicon atoms that are not properly bonded to the lattice. We assume they have a different orientation, even when our model still places them in the perfect lattice site (recent research is trying to overcome this limitation, see [5]). Defective atoms serve as recrystallization seeds that propagate the alternative orientations.

Our model assumes that only {111} recrystallizations can introduce defective atoms in the simulation. They are assigned a probability P_{def} of changing the orientation. The physical mechanism that links the {111} recrystallization to defect introduction is the formation of twins. These twins are formed by the rotation of the middle atom in a {111} microscopic recrystallization giving a different lattice orientation that is locally compatible with the {111} plane. The parameter P_{def} can be controlled with

```
pdbSet KMC Silicon Damage
probability.SPER.defect
```

and it is set to 75% by default. Much smaller values for P_{def} do not produce enough defects, and larger values can stop the {111} recrystallization and produce compact defective silicon instead of twinning.

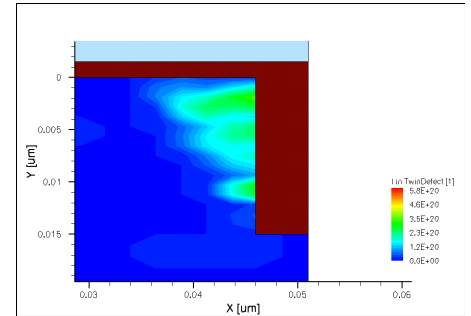


Figure 5: Concentration of defective silicon close to a SiO₂ trench.

Figure 5 shows the concentration of defective silicon (reported under the name TwinDefect in the Sentaurus output file) near a SiO₂ trench. An area of defective silicon, limited by a {111} plane is formed, in good agreement with experimental results.

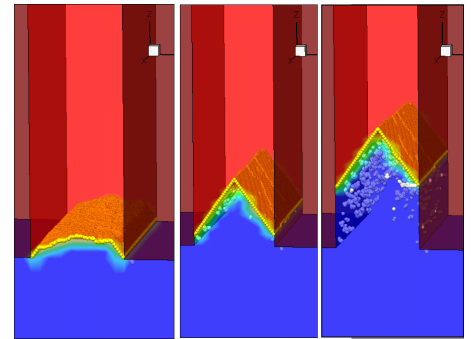


Figure 6: SPER inside a thin fin, showing the defect formation (white atoms).

Figure 6 shows the evolution of SPER in a thin fin. The characteristic “arrow shape” is formed by the creation of {111} planes limited by the SiO₂ on both sides. After the {111} planes are formed, recrystallization continues, but it is very defective.

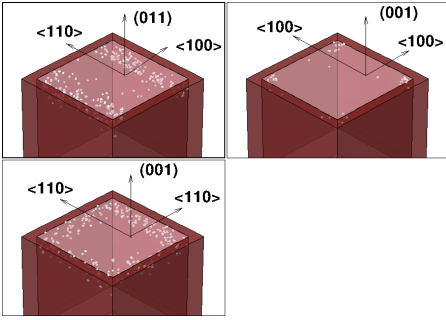


Figure 7: Different defect formation after SPER of rectangular amorphized shapes at different substrate and lateral orientations.

Finally, Figure 7 shows defect formations after SPER of rectangular amorphized shapes at different substrate and lateral orientations. The agreement with experiments is excellent [6]. For substrates with (011) orientation and <100> alignments, two stripes of defects close to the lateral boundaries along the <110> direction can be seen in both experiments and simulations, while in (100) substrates with <011> alignments, the defects surround all the edges. Interestingly, also in both simulations and experiments, defects can be confined to the four corners if a (100) substrate orientation is aligned in a <001> direction instead of <011>.

Save and load defects from and to text files

Two new commands have been added to allow the saving and loading of particles and defects from ASCII files. The commands are `defects.read` and `defects.write`.

These commands take only one argument, the filename to read or write the defect type and position:

```
kmc defects.read=defects.dat
```

takes the defects in the simulation and writes them in a file (`defects.dat` in this example), while

```
kmc defects.write=defects.dat
```

takes the defects written in a file and inserts them in the simulation.

This command is similar to `kmc add`, except that it takes the defects from a text file. For extended defects only, the center of mass of the defect is written or read. This feature is not intended to replace `tdr` file read or write, but to allow users to read defects (for instance, cascades) generated by other means, or to create easy-to-process ASCII output files for customized post-processing. For physical restarting, `tdr` files that store all the particles of extended defects instead of the size and center only should be used.

An example of the format of the read and created files for defects is:

| | | | | |
|-----------------|------|-----------|-----------|-----------|
| ImpurityCluster | B3I2 | 4.797926 | 5.482407 | 4.881657 |
| ImpurityCluster | B2I | 6.878131 | 6.481280 | 7.694045 |
| PointDefect | Bi | 26.000000 | 26.000000 | 26.000000 |
| ThreeOneOne | I100 | 19.554871 | 20.445129 | 20.000000 |
| Loop | PI59 | 13.000000 | 13.000000 | 13.000000 |
| PointDefect | BiM | 30.000002 | 5.000000 | 14.000000 |
| ThreeOneOne | I50 | 10.000000 | 10.000000 | 10.000000 |
| Interface | P | 1.000000 | 11.250000 | 13.000000 |
| PointDefect | As | 5.032000 | 5.320000 | 1.032000 |
| PointDefect | B | 10.000000 | 5.000000 | 6.000000 |
| PointDefect | Ge | 6.696747 | 7.492962 | 0.834044 |

The first column contains the generic defect name, second the name of the particular defect (including the size), with the defect center coordinates indicated by the third, fourth and fifth columns. Complex cases, such as the small dislocation loop (59 interstitials) that is decorated with 1 phosphorus atom (P) are also supported (PI59)

Better extract interface for amorphous/crystalline interfaces

The command `kmc extract acinterface` has been adapted to use the atomistic information instead of the internal mesh elements when the LKMC model is being used for SPER. This increases the accuracy of amorphous/crystalline (A/C) interface information and prevents some numerical fluctuations that were common when using the internal elements information.

If the user is not using LKMC models for SPER, the command does not have atomistic information for the A/C interface and still uses the internal KMC mesh element information.

Sentaurus Device

Enhancements to the auto-orientation framework

Density-gradient quantization model

The auto-orientation framework in Sentaurus Device has been extended to work with the density gradient quantization model. This

allows Sentaurus Device to automatically switch between different orientation-dependent parameter sets for the density gradient model based on the surface orientation of the nearest interface. This is an important feature because it is known that quantization in devices depends on surface orientation. It is especially relevant for the simulation of devices such as FinFETs that can have channels with multiple surface orientations.

As an example, Sentaurus Device is used to obtain the hole density distribution in the cross-section of a p-channel FinFET biased in strong inversion. The FinFET features a fin width of 20 nm, channel doping equal to $3 \times 10^{18} \text{ cm}^{-3}$, and a gate oxide thickness of 1 nm. The device is oriented such that the top surface is (100) and the side surfaces are (110). The density gradient quantization model with auto-orientation is used for the simulation. The orientation-dependent



density gradient γ_n parameters were obtained by calibrating against S-Band Schrödinger calculations ($\gamma_n(110) = 3.3$, $\gamma_n(100) = 8.3$).

The results of the simulation are shown in Figure 8. The left plot shows the 2D hole density distribution in the device. The different quantization behavior along the top and side surfaces is evident. This can be more clearly seen in the 1D cutline plots shown on the right. The hole distribution profiles along the side (110) surfaces are higher and more narrow than the hole distribution profile along the top (100) surface.

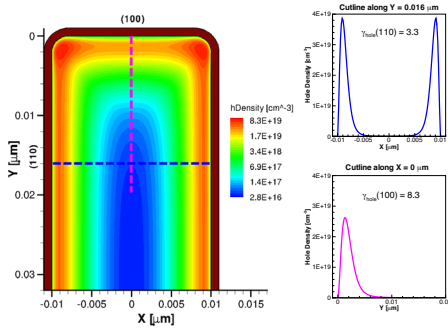


Figure 8: Hole density distribution in a 2D cross-section of a p-channel FinFET biased in strong inversion and corresponding 1D cutline plots through the structure.

Auto-orientation smoothing

The auto-orientation framework has been enhanced to provide a smooth spatial transition between different orientation-dependent parameter sets during model evaluation. Previously, Sentaurus Device would switch abruptly from one parameter set to the next, potentially resulting in abrupt spatial changes of physical quantities such as mobility. The auto-orientation smoothing distance, which controls the extent of the transition between parameter sets, can be specified by the user. Alternatively, an automatic calculation of the smoothing distance can be invoked, which is optimal for most cases. This feature works with all auto-orientation enabled models.

InterfaceCharge mobility model enhancement

The InterfaceCharge mobility model in Sentaurus Device provides a simple means of including mobility degradation due to remote Coulomb scattering (RCS) in a device simulation. The model can be used in addition to other mobility models (for example the enhanced Lombardi model) and provides an explicit dependence on both the magnitude and location of trapped- or fixed-charge scattering centers in the structure.

For the G-2012.06 release, the InterfaceCharge model has been extended to include dependencies on impurity concentration. This extension provides additional flexibility when calibrating simulation results with experiment data.

“Atomistic” workfunction randomization in metal gates

The workfunction in metal regions now can be randomized using specifications in the command file. The approach taken assumes that the metal consists of randomized grains of varying size and shape that can be characterized with a user-specified average grain size. Grain workfunction values and probability statistics can be specified to model the behavior of different materials.

As an example, Figure 9 shows the electrostatic potential in an n-channel MOSFET where the workfunction in the metal gate has been randomized. The figure also shows the electrostatic potential in the metal gate for three other randomizations.

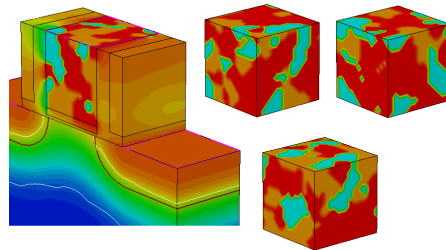


Figure 9: Electrostatic potential in an n-channel MOSFET where the metal gate workfunction has been randomized. Also shown is the electrostatic potential in the metal gate for three other randomizations.

Speed-up of stress models for holes

The hSubband model for the calculation of orientation and stress dependent mobility gain has been sped-up when used in conjunction with the Doping option. During bias ramping, the model now runs as quickly as other stress-related mobility models. In addition, a new Save/Load option for the pre-computation of the six-band **k.p** density and hSubband mobility data has been implemented. This option allows users to compute the required density and mobility data once and then re-use the data for subsequent Sentaurus Device simulations. Also, the multi-valley model for carrier density has been parallelized to improve wallclock time with multiple threads.

Variability analysis with the impedance field method

With decreasing device feature sizes, random variations of device properties become increasingly important. It is generally recognized that the most important source of variability is due to random doping fluctuations (RDF), where the exact number and position of the individual dopants affects the properties of a device. Sentaurus Device has been able to model RDF with the impedance field method (IFM) for several years now.

In the impedance field method (IFM), the currents and voltage variations for a device are computed in linear response to a variation of the device, such as the variation in the placement of dopants. The linearization allows for a drastic reduction in the computational effort to model variations as compared to the atomistic approaches prevalent in the academic literature. In these atomistic approaches, a large number of devices with random variations are generated, and for each of these devices, a complete device simulation is performed. This creates a computational burden that is hardly affordable for industrial users. Furthermore, the full atomistic treatment, in



the case of RDF, is not compatible with the continuous device models usually employed in TCAD, which makes the atomistic modeling of variability a task disconnected from all other modeling tasks.

Modeling of metal grains with IFM

As the industry transitions to metal gates, a second highly important source of variability has emerged: random workfunction fluctuations (RWF) due to the formation of finite-sized metal grains with different lattice orientations.

If one assumes that the metal grains responsible for RWF are large compared to the device feature sizes, they are easy to model: The workfunction shift is uniform over a contact and, therefore, has the same effect as a variation of the voltage applied to the contact. In such cases, conventional small-signal analysis is sufficient to model the effect of large metal grains.

If the metal grain size is smaller or on the order of the device feature size, this simple approach no longer works. Release F-2011.09 allowed the usage of Physical Model Interface (PMI) to implement an atomistic approach to model RWF for arbitrary grain size. While in the case of RWF no incompatibility with continuous TCAD models exist, the issue of high computational burden remains.

For this reason, in version G-2012.06, Sentaurus Device offers RWF modeling based on the IFM. Two variants of IFM modelling are supported: The statistical IFM (sIFM) and the noise-like IFM (nIFM).

The sIFM is close to the atomistic method and, therefore, easy to understand. Like in the atomistic method, the device structure is randomized. For RWF, metal grains are randomly generated and workfunction values are randomly assigned to these grains. But in contrast to the atomistic approach, the randomized structure is not directly used to perform a full simulation. Instead, after randomization, the deviation of the

randomized structure from the average structure is obtained. For RWF, for each point in the metal this yields the difference of the workfunction for the grain to which this point belongs relative to the average workfunction. Finally, the effect of the deviation on device currents and contacts is computed in linear response.

For the sIFM, a large number of random samples is created, and for each of them, current and voltage curves are obtained. Thanks to the efficiency of IFM, thousands of samples are easily affordable. The curves obtained can then be analyzed to obtain insight into effect of RWF.

The second approach for RWF is the nIFM. In the nIFM, the device structure is not randomized, but a correlation function (called "noise source") for the varying quantity is assumed. The noise source describes how the workfunction in one point is related to the workfunction in another point. The model implemented in Sentaurus Device assumes that the spatial correlations are Gaussian.

The nIFM does not have to perform multiple randomizations and, therefore, is potentially faster than the sIFM and is not affected by errors that would arise from a too small sample size. It also produces its results in a compact form as the variances of contact currents and voltages. This makes post-processing easier compared to sIFM, but also more restricted, as higher-order statistical moments are not available. The most severe disadvantage of nIFM compared to sIFM is not technical: due to the higher level of abstraction, it is more difficult to understand and interpret the nIFM results.

Modeling of trap concentration variations with IFM

Another new feature in version G-2012.06 is the support for the modeling of random trap concentration fluctuations (RTF). Both sIFM and nIFM are supported. Conceptually, RTF are similar to RDF. In both cases, the origin of the variations is the discreet nature

of atoms, and the fact that their exact placement affects device properties. Due to this similarity, the statistical model for RTF is the same than for RDF, namely, all traps are considered uncorrelated.

Other than for RDF, for the RTF modeling, there is no effect of the trap placement on bandgap narrowing and on mobility. On the other hand, the relation of trap concentration on trap-related recombination-generation is well-defined and, therefore, included in the RTF modeling approach. All recombination-generation processes are supported, including nonlocal trap tunneling. This allows, for example, the simulation of the impact of trap concentration variations on trap-assisted leakage current through insulators.

Improvements in thermoelectric transport

Thermal boundary resistance model

A new distributed thermal resistance at the interface between two materials has been introduced to allow resistive heat transfer between two regions. The feature can be used at semiconductor/semiconductor, insulator/insulator and semiconductor/insulator interfaces.

A thermal boundary resistance at interfaces could also be emulated by inserting a thin layer with a specific thermal resistivity between the two materials, but this approach is practical only for relatively flat interfaces. The new distributed thermal resistance removes this limitation for the type of interfaces mentioned above.

A direct application of the new feature is the study of the effect of thermal boundary resistance (TBR) in phase-change memory devices. Figure 10a shows how a thermal boundary resistor at the GST/oxide interface shifts the region where the maximum temperature occurs. Figure 10b shows the discontinuity in temperature occurring at GST/oxide interface when thermal boundary resistance is considered.

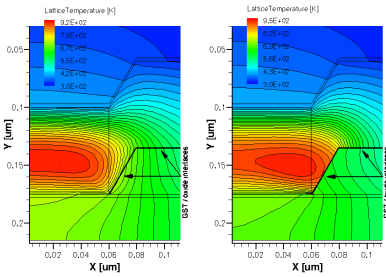


Figure 10a: Temperature profiles for reset simulations with no TBR and with TBR=0.001 Kcm²/W.

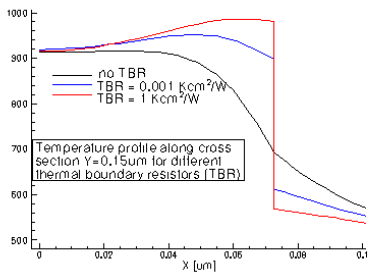


Figure 10b: Temperature profile cross-section along Y=0.15um for different thermal boundary resistors (TBR).

Thermoelectric power PMI

A new physical model interface (PMI) for thermoelectric powers has been introduced for semiconductors and metals. Using the new PMI, the user can define new thermoelectric power models as functions of carrier density and lattice temperature in semiconductors and as functions of electric field and lattice temperature in metals.

Thermodynamic transport in metals

Continuity and heat conduction equations in metals have been generalized to include thermodynamic transport (temperature gradient driven current component) and heat flow due to thermoelectric power.

As an example, in Figure 11a and Figure 11b the new feature is used to simulate the Seebeck effect in a bimetal temperature sensor. The temperature at the tip of the device is sampled by measuring the voltage difference between the two electrodes kept at 300K. Figure 11a shows the temperature and potential profiles when the sensing

tip is kept at 500K. Figure 11b shows the thermocouple voltage-temperature (V-T) curve. The thermoelectric powers in the two metals were modeled as linear functions of lattice temperature.

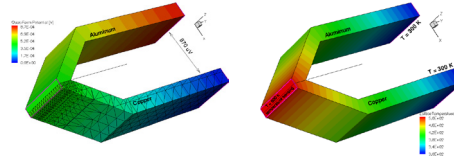


Figure 11a: Temperature and potential profiles in an Al/Cu thermocouple. The tip of the thermocouple is kept at 500K and the thermoelectric power is measured between the two electrodes kept at room temperature.

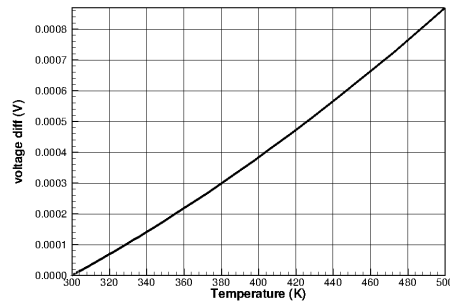


Figure 11b: Thermocouple voltage drop as a function of measured temperature.

MOS harness for compact modeling

Sentaurus Device provides many HSPICE MOSFET compact models for mixed-mode simulations. Some of these models feature self-heating capabilities, such as the level 57 and 59 BSIM3-SOI models, the level 62 RPI Poly-Si TFT model, or the level 73 STARC HiSIM-LDMOS/HiSIM-HV model. These models can be included directly into an electro-thermal simulation. However, other HSPICE models lack this capability, and thus they are not immediately available for electro-thermal simulations.

In this release we introduce a MOS harness as a wrapper around a MOSFET to capture the power P and inject it as a heat flux

into the thermal circuit. The power P of a standard four-terminal MOSFET is given by

$$P = i_d u_d + i_g u_g + i_s u_s + i_b u_b$$

where i_d , i_g , i_s , i_b denote the drain, gate, source, and bulk currents, respectively, and u_d , u_g , u_s , u_b denote the drain, gate, source, and bulk voltages, respectively.

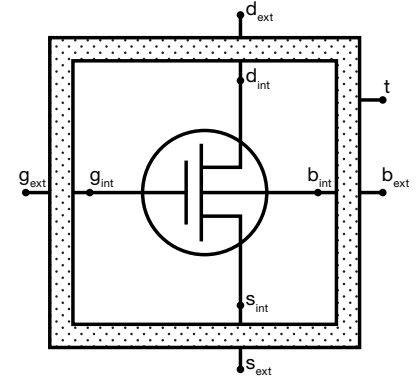


Figure 12: MOS harness.

The harness shown in Figure 12 acts as an interface between the MOSFET and the rest of the circuit. The four internal electrodes d_{int} , g_{int} , s_{int} , and b_{int} are connected to the MOSFET to monitor the voltages and currents at the four electrodes. The four external electrodes d_{ext} , g_{ext} , s_{ext} , and b_{ext} connect the device electrically to the rest of the circuit. Finally, the thermal contact t feeds the power generated by the MOSFET into the thermal circuit.

Figure 13 shows a sample circuit to measure the power produced by an HSPICE MOSFET. The HSPICE model computes the contact currents which are passed on transparently into the electrical circuit. At the same time the MOS harness computes the power P and sends it as a heat flux to the thermal resistor R_{th} . The thermal resistor R_{th} is connected to V_{th} which models an external heat sink of constant temperature. The self-heating of the MOSFET can now be analyzed by monitoring the temperature at the thermal node of the MOS harness.

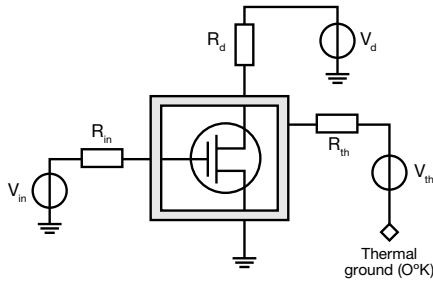


Figure 13: Sample electrothermal circuit.

The MOS harness is available as a compact model both in Sentaurus Device and in Sentaurus Interconnect.

Optoelectronic enhancements

Several enhancements to the unified optical generation interface have been developed. Logarithmic interpolation is enabled for the wavelength dependent complex refractive index table. The unified raytracer is now able to utilize the concept of illumination window such that multiple excitation shapes can be defined. These shapes include lines for 2D, and rectangles, circles and polygons for 3D. For each excitation shape, different types of ray distribution can be chosen to facilitate the specification of complex light sources. The parameters of the illumination windows are rampable so that we can even simulate a moving light source. Farfield plotting and external sensors have also been added to the unified raytracer and users will be able to measure the accumulated photons exiting from the device in a number of ways. This will expedite the computation of reflection and other design quantities.

Release G-2012.06 also includes several enhancements to Sentaurus Device EMW. The parallel licensing options in EMW have been revamped to allow users to specify wait in queue or abort states, depending on license availability. Selective final EMW results can be saved, and users will be able to consequently apply Plot/Extractor/Sensor in postprocessing mode to rapidly extract necessary slices of the final results without having to re-run the entire FDTD simulation.

EMW results can also be saved in a tensor format that contains region information so that interfaces can be shown in Sentaurus Visual (see Sentaurus Visual section at the end of this newsletter for more information about this new visualization tool).

Sentaurus Device Monte Carlo

3D Monte Carlo device simulation

Since further scaling requires suppression of the short-channel effect, FinFETs have been introduced due to their effective channel control in a multi-gate architecture. For predictive device simulation, this involves several new challenges compared to the simulation of bulk MOSFETs: (i) FinFETs are inherently three-dimensional devices and involve geometric features such as corner rounding or pronounced sidewall angles which can only be resolved by unstructured device meshes, (ii) a physical model for surface scattering is needed which is valid for arbitrary crystallographic surface orientations (not only for the typically different orientation of sidewall and top surface, but also for the unconventional orientations arising at the fin corner regions and for non-zero sidewall angles), (iii) quasi-ballistic overshoot effects must be considered because FinFETs are used at even shorter gate lengths of 20 nm and below and (iv) simulation times must be short enough to allow for the investigation of performance trends as a function of geometry, orientation and stress. In order to provide such a device simulation capability, the single-particle Monte Carlo approach has been extended in release G-2012.06 to also handle 3D devices.

Orientation dependence of the effective mobility

Figure 14 shows Monte Carlo results for the effective long-channel mobility in a FinFET for $\langle 110 \rangle / \langle 110 \rangle$ and $\langle 100 \rangle / \langle 100 \rangle$ orientation of channel and sidewall in comparison to recent experimental data [7].

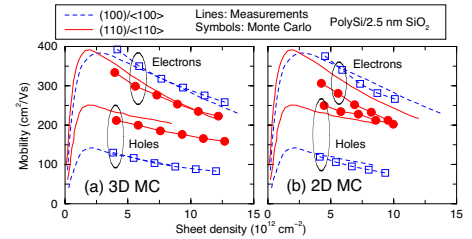


Figure 14: Long-channel effective electron and hole mobilities in a FinFET with gate length $L=0.5\mu\text{m}$, fin height $H=40\text{nm}$, fin width $W=30\text{nm}$ and a nitride hard mask on top of the fin. Measurements [7] are compared with (a) 3D Monte Carlo and (b) 2D Monte Carlo simulation referring to a double-gate device obtained from a horizontal cut through the FinFET.

The effective mobility is computed via

$$\mu_{eff} = \frac{L I_D}{W_{eff} q N_{inv} V_D}$$

where L is the gate length, I_D the drain current, W_{eff} the effective gate width (taken as twice the fin height H because of the nitride hard mask on top of the fin), N_{inv} the inversion sheet density (per gate area) and $V_D=50\text{mV}$ the drain voltage.

It can be seen that 3D Monte Carlo simulation is able to reproduce the measured orientation dependence of the effective mobility. This orientation dependence originates from the model for surface scattering which consists of a combination of 85 % specular and 15 % diffusive scattering. The specular part is governed by conservation of parallel crystal momentum and energy when a carrier hits the surface. In the case of an isotropic band structure, this leads to the familiar situation where the angle of reflection is equal to the incident angle. However, for anisotropic band structures, the two conservation laws allow also a complete reversal of the parallel group velocity component and, therefore, a reduction of the mobility. A more detailed discussion of this effect can be found in the literature [8,9].



Interestingly, 2D Monte Carlo simulation involves for the $\langle 110 \rangle / \langle 110 \rangle$ configuration a higher hole and a smaller electron mobility, respectively. This is due to a significant fraction of carriers traveling along the $\langle 100 \rangle$ oriented top surface despite the presence of the nitride hard mask and demonstrates that even in this case 3D simulation is mandatory to capture the physical behavior correctly.

Short-channel FinFET simulation

Figure 15 shows the geometry of a 15nm FinFET where a stressor cap liner is considered in analogy to a recent experimental investigation [10].

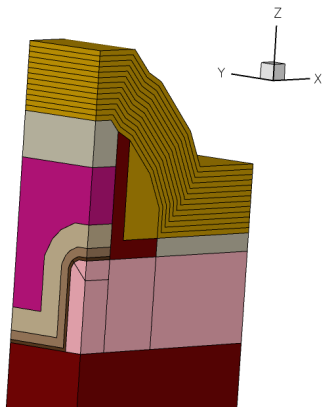


Figure 15: Geometry of a FinFET with gate length $L=15\text{nm}$, fin height $H=20\text{nm}$, fin width $W=8.5\text{nm}$ and a 15nm thick cap layer.

The velocity profiles along the channel can be seen for the on-state in Figure 16. They correspond to on-currents of 806 and 713 $\mu\text{A}/\mu\text{m}$ with and without stress, respectively, for the same gate-over drive in the case of nFinFETs (558 and 478 $\mu\text{A}/\mu\text{m}$ for pFinFETs with a higher threshold voltage). It turns out that electrons travel along the whole channel with a velocity far higher than the saturation velocity of $1 \times 10^7 \text{ cm/s}$. Nevertheless, stress is still effective to further enhance the velocity in the source-side of the channel and therefore also the on-current.

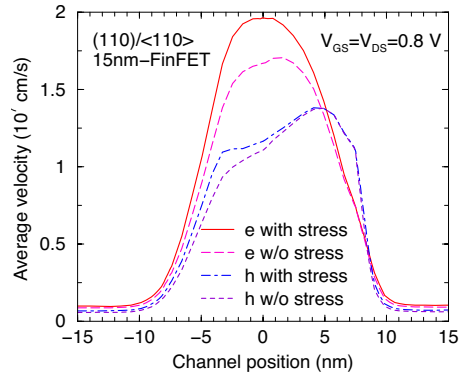


Figure 16: Velocity profiles along the channel in the short-channel FinFET. Stress is due to a 15nm thick cap layer with 2 GPa intrinsic stress. The velocities are averaged with the carrier densities over the cross-section of the fin.

Parallelization

The final aspect of 3D Monte Carlo device simulation concerns the computational speed which can be achieved together with parallelization. Typical wallclock times for a statistical error below 2 % are about one hour with 12 cores for long-channel I_{dlin} (used to compute the effective long-channel mobility) and less than half an hour with 8 cores for short-channel I_{dsat} on a 2.93 GHz Intel Xeon CPU X5670. The corresponding memory consumption is 6.8 GByte and 6.1 GByte, respectively, arising for a tetrahedral mesh of about 918,000 elements and 192,000 vertices for the long-channel device and 467,000 elements and 102,000 vertices for the short-channel FinFET. These short wallclock times for 3D Monte Carlo simulation are possible thanks to the single-particle approach to self-consistent Monte Carlo device simulation [11] where a stationary solution of Boltzmann and Poisson equations is obtained via an iterative scheme. This involves only about 20 Poisson updates, so that the increase in node count in 3D does not present a problem.

Subband and inversion-layer mobility calculator

Several new features have been added to Sentaurus Band Structure (S-Band) to enhance the calculation of inversion-layer mobility.

Silicon mobility calculations

To improve the accuracy of electron mobility calculations for the $\langle 110 \rangle$ and $\langle 111 \rangle$ surfaces, the Schrödinger solver has been generalized to account for the impact of non-parabolicity on quantization. In addition, new default parameters for both electron and hole mobility calculations in silicon have been established in order to improve the accuracy of mobility calculations over a wide range of conditions including orientation, strain, and doping. For example, Figure 17 demonstrates the effectiveness of using a relatively high non-parabolicity value for quantization in reproducing experimentally measured $\langle 110 \rangle$ electron mobility for both the $\langle 110 \rangle$ and $\langle 100 \rangle$ channel directions with a single set of scattering parameters.

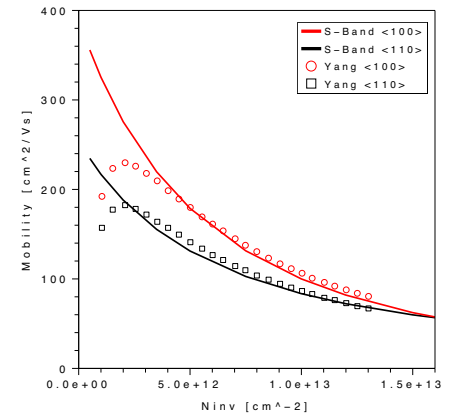


Figure 17: Comparison of electron mobility calculations in S-Band to experimental data [12] for $\langle 110 \rangle / \langle 110 \rangle$ and $\langle 110 \rangle / \langle 100 \rangle$ orientations.

Framework for SiGe hole mobility calculations

Several enhancements have been made to enable the calculation of hole mobility in SiGe heterostructure devices. In particular, for the 6-band $\mathbf{k}\cdot\mathbf{p}$ Schrödinger equation



(SE), a new discretization approach has been implemented in order to eliminate spurious solutions at interfaces. In addition, more general scattering models have been implemented to treat multi-layer quantum wells, the weighted contribution of phonons from both Si and Ge, and elastic alloy scattering. Mobility can be computed for arbitrary mole fraction, surface orientation, and stress. As shown in Figure 18, good agreement is obtained with measured data for the hole mobility in a pure Ge (100)/<110> device.

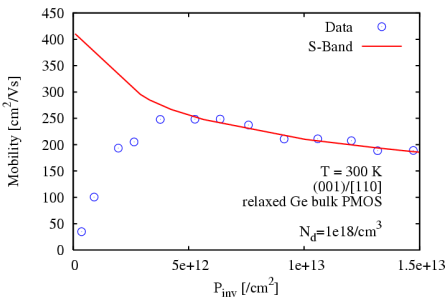


Figure 18: Comparison of calculated mobility in S-Band to measurements of hole mobility in a relaxed Ge bulk pMOS device with a doping concentration of $1e18/cm^3$ [13].

Other enhancements

Contact resistance

Contact resistance now can be included in Monte Carlo simulations. As in drift-diffusion simulation, both lumped and distributed resistances can be specified in the Electrode section of the Sentaurus Device input file. In this case Poisson and contact equations will be solved self-consistently after each Monte Carlo carrier propagation step. A voltage drop corresponding to the Monte Carlo current sets boundary conditions for the Poisson equation.

Current evaluation via particle counting

In release G-2012.06, the current is now estimated by default via particle counting instead of using the test function method. This improves especially the simulation of the subthreshold regime.

Sentaurus Interconnect

Enhancements to fracture mechanics

Fracture mechanics comprises several important features with application to key industry problems such as chip-package interaction (CPI). Cracks occur in materials due to several reasons. Depending on the location of the crack, manufacturing process steps, and operating conditions of the semiconductor device, small cracks may propagate to become large cracks and cause failure. Therefore, it is critical to understand how cracks affect the performance and reliability of semiconductor devices. Fracture mechanics capabilities in Sentaurus Interconnect provide several tools to define and simulate crack propagation.

When crack propagation occurs along a predefined path in 2D and 3D structure, as in interface cracks, the cohesive zone material (CZM) model [14] is used. Traction-separation laws are provided to model the variation of normal and shear tractions with normal and tangential separation of crack surfaces. For more general cases where the crack path depends on loading and boundary conditions, linear elastic fracture mechanics (LEFM) theory is used to predict crack propagation. Energy is released when a crack front advances to create new surfaces. This energy release rate can be calculated with the so-called J integral [15] formulation and then compared against the fracture toughness of the material. Sentaurus Interconnect provides a domain integral based capability to compute the J integral [16] for cracks in 2D and 3D structures.

J integral for an edge crack in a 3D block

To demonstrate the J integral capability, we consider a 3D rectangular block of height $H=10\mu m$, width $W=5\mu m$ and thickness $B=0.25\mu m$ and an edge crack of length $a=1\mu m$ on the right side as shown in Figure 19. The block is fixed on the left by applying Dirichlet boundary conditions. The crack is assumed to be initially closed without

any resistance to opening in the normal or tangential direction. To simulate a mode I crack opening, normal traction $\sigma=1 MPa$ is applied on top and bottom surfaces. The block is assumed to be made of Aluminum with Young's modulus $E=85.6 GPa$ and Poisson's ratio $\nu=0.289$. Stresses build up around the crack tip under applied tractions.

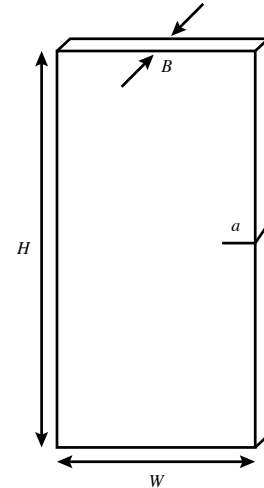


Figure 19: 3D block with edge crack.

A stress analysis is performed in Sentaurus Interconnect by applying the velocity and distributed force boundary conditions on a 3D model of the block. Figure 20 shows the YY component of stresses in the deformed 3D block. J integral calculations for the edge crack are performed using the domain integral method which uses the stresses and elastic strain energy density saved during the stress analysis. For the 3D crack, J integral values are computed at various points along the crack front by specifying the coordinates of these points. An average of all the J integral values along the crack front is also calculated automatically. Since the stresses around the crack front typically have very high gradients that are not represented accurately by the linear tetrahedral finite elements, J integral values are computed over multiple domains. The first domain consists of those elements that share nodes with the crack front. Each subsequent



domain contains elements from the previous domain and elements that share nodes and edges with the previous domain.

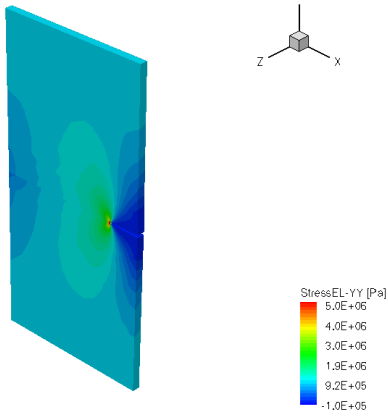


Figure 20: Stress-YY for 3D block with edge crack.

To verify the accuracy of the numerical scheme, J integral values are compared against an analytical solution for energy release rate. For an edge crack in a plate where $\frac{a}{w} \geq 1$, the energy release rate for mode I is given as

$$G_{\text{plane strain}} = \frac{(1-\nu^2) f^2 \sigma^2 \pi a}{E}$$

where

$$f = 1.122 - 0.231\left(\frac{a}{w}\right) + 10.55\left(\frac{a}{w}\right)^2 - 21.71\left(\frac{a}{w}\right)^3 + 30.382\left(\frac{a}{w}\right)^4$$

Using the dimensions of the 3D block, crack length and material properties, the value of energy release rate comes out to be

$$G_{\text{plane strain}} = 6.338 \times 10^{-5} \text{ N/m.}$$

Table 2 lists the ratio of J integral value to energy release rate at various points along the crack front and over various domains. The average values in the last column show a good agreement between numerical and analytical solution.

Temperature-dependent compact models

In the G-2012.06 Sentaurus release, mixed mode analysis in Sentaurus Interconnect has been expanded to include temperature dependence with electrical analysis via specification of thermal elements. A thermal element is a circuit element attached to thermal nodes or to a combination of thermal and electrical nodes. These elements are capable of getting thermal feedback through the device and vice-versa. As previously, electrical and thermal nodes can be connected to the structure through contacts. An additional feature allowing connecting multiple nodes (thermal and electrical) to a single contact is provided. Dirichlet boundary conditions can be set on thermal nodes. A fixed value thermal node should have non-zero and realistic value to avoid convergence problems.

The new feature is demonstrated in a three-dimensional damascene structure as shown in Figure 21. The copper wire is connected virtually to the drain of a transistor, which is a 90nm SOI n-type MOSFET defined in

the HSPICE model (Level 57 UC Berkeley BSIM3-SOI Model). The model has a thermal node which feedbacks the temperature of the individual transistor. This thermal node is connected virtually to the silicon surface and heats up the whole damascene structure. The potential and heat equations are solved in a coupled manner to accurately simulate the interaction of current and temperature. Figure 22 shows distribution of electrical current density (left) and temperature (right).

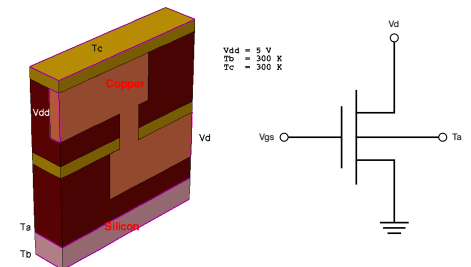


Figure 21: (Left) Three-dimensional damascene structure with copper interconnect and silicon substrate. (Right) The circuit attached to the structure.

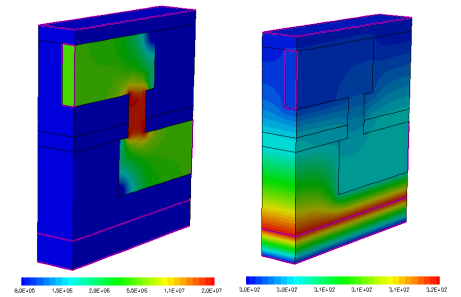


Figure 22: (left) Electrical current density and (right) temperature distributions.

| Domain | z=0.0 | z=B/8 | z=B/4 | z=3B/8 | z=B/2 | z=5B/8 | z=3B/4 | z=7B/8 | z=B | Average |
|--------|-------|-------|-------|--------|-------|--------|--------|--------|-------|---------|
| 1 | 0.880 | 0.955 | 1.024 | 1.049 | 1.061 | 1.068 | 1.075 | 1.086 | 0.970 | 1.019 |
| 2 | 0.938 | 1.007 | 1.062 | 1.083 | 1.093 | 1.097 | 1.098 | 1.089 | 0.968 | 1.048 |
| 3 | 0.968 | 1.024 | 1.076 | 1.096 | 1.105 | 1.108 | 1.106 | 1.091 | 0.952 | 1.059 |
| 4 | 0.983 | 1.031 | 1.082 | 1.101 | 1.110 | 1.112 | 1.109 | 1.093 | 0.943 | 1.063 |
| 5 | 0.991 | 1.034 | 1.085 | 1.104 | 1.112 | 1.114 | 1.110 | 1.094 | 0.937 | 1.064 |

Table 2: $J/G_{\text{plane strain}}$ for an edge crack in a 3D block of thickness $B=0.25 \mu\text{m}$ and $G_{\text{plane strain}}=6.338 \times 10^{-5} \text{ N/m}$



Enhancements to boundary conditions

Sentaurus Interconnect provides several different types of boundary conditions for mechanics: velocity (displacement rate), total force and distributed force. These boundary conditions are specified on the outer boundary surfaces of the simulation domain or contacts. The prescribed values of the boundary conditions are applied from the start and kept constant for the entire solve step.

In Sentaurus Interconnect G-2012.06, two new options are being added to boundary conditions.

Temperature and time dependent boundary conditions

Boundary conditions for velocities, total forces and distributed forces can now be made dependent on temperature and time using procedures. Users can write a separate procedure for each component. As an example, consider a 2D block (5 μm x 10 μm) with bottom half being silicon at 400 K and top half being aluminum at 300 K. Left and bottom boundary surfaces are assumed to have zero normal velocities. Temperature dependent velocity is specified on right boundary surface using the `stressdata` command with a procedure:

```
stressdata bc.location=Right
bc.proc= {dyP=LookUpTable}
proc LookUpTable { args } {
  set CurrTemp [lindex $args
0] ; #current temperature in C
  set dy 0
  if { $CurrTemp < 27 }
  {
    set dy 1.0e-5 ;
  }
  #velocity in cm/s
} elseif { $CurrTemp > 27
&& $CurrTemp < 127 } {
  set dy 1.0e-6 ;
}
#velocity in cm/s
} else {
  set dy 0 ; #velocity in
cm/s
}
return $dy
}
```

Figures 23 and 24 show the temperature and displacement plots on deformed configuration, respectively.

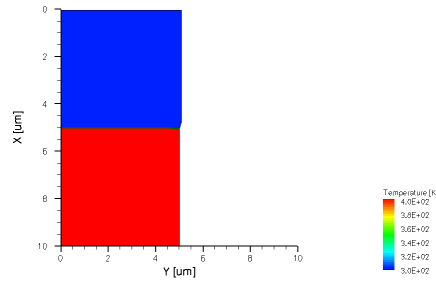


Figure 23: Temperature in 2D block with temperature dependent velocity boundary condition

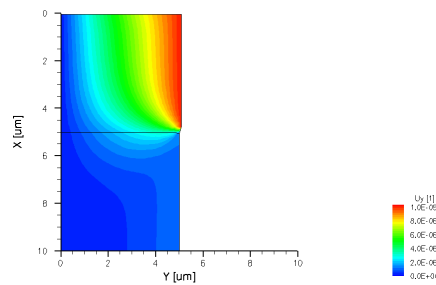


Figure 24: Displacement Uy in 2D block with temperature dependent velocity boundary condition

The temperature difference between the two halves of the block leads to different velocities on the right boundary surface.

Point-displacement rate boundary condition

This new boundary condition allows velocity (displacement rate) to be specified directly at a bulk node. Users must provide the coordinate of the bulk node along with the values of components of velocity (displacement rate). If a bulk node is not located at the specified coordinate, the nearest node is picked based on snap tolerance. The default value for snap tolerance is 1nm and can be modified by the user. To demonstrate this boundary condition we use the 2D block from previous example. We fix the velocities on the bottom boundary surface and apply point-

displacement rate boundary condition on top surface at a point with coordinates $x=0.0 \mu\text{m}$, $y=2.5 \mu\text{m}$, $z=0.0 \mu\text{m}$:

```
stressdata bc.location=PointBC
bc.value= {pdx=2e-4} point.
coord= {0.0 2.5 0.0}
```

Figure 25 shows the displacement contours on deformed configuration of the 2D block.

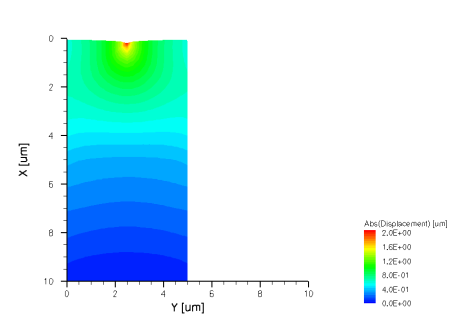


Figure 25: Displacement magnitude in 2D block with point-displacement rate boundary condition

Displacement contours verify the application of the boundary condition at the bulk node closest to the specified point coordinate.

Sentaurus Mesh

Improvements to offsetting module

With previous releases, when `-offset` option was used for the offsetting feature, the elements inside the layers were not fully refined according to the user-requested specifications in the command file. Doping-based refinement would be completely lost inside the layers, leaving gaps which could only be filled with an isotropic refinement post-processing step (added in the last release). The isotropic refinement option refines the elements within layering isotropically without considering the layering direction. Due to the nature of isotropic refinement, the element count could grow dramatically, and be impractical in some situations. To address this problem, in G-2012.06 we are introducing a new option which performs anisotropic refinement in the



layers, both in 2D and 3D. This new option refines elements inside the layers by taking into account the local orientation of the layers.

The elements inside a layer are refined either normal or parallel to the layers. By considering the local layer orientation, the resulting refinement is now similar to the default axis-aligned refinement, with the only difference that the elements are not necessarily axis-aligned but follow the orientation of the layers. In addition to that, the element count in a mesh will be greatly reduced when compared to mesh generated using isotropic refinement option.

A trench example is provided to demonstrate both the refinement options. Figure 26a shows mesh generated with offset option but without any refinement option. In this figure, the elements inside the layers don't satisfy the refinement specifications in the command file. Figure 26b shows the mesh with 4927 elements generated with isotropic refinement. Figure 26c shows the mesh with 2995 elements generated using anisotropic refinement. By comparison, the mesh generated with the anisotropic refinement option requires fewer elements to satisfy the refinement specifications.

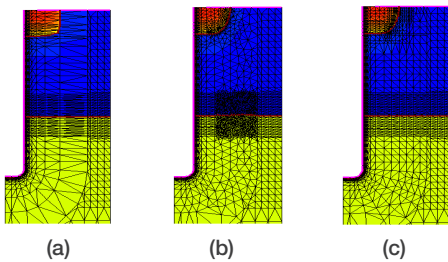


Figure 26: (a) Trench structure with mesh generated with the offset option but no refinement option, (b) trench structure with mesh generated with isotropic refinement, and (c) trench structure with mesh generated by anisotropic refinement.

Sentaurus Visual

Overview

Sentaurus Visual is a new addition to the TCAD Sentaurus product family. It is designed to address the growing importance for visualization and analysis of semiconductor one-dimensional (1D), two-dimensional (2D) and three-dimensional (3D) structures, as well as their X/Y data. Sentaurus Visual is a new generation of visualization tool, with the focus on a friendly and easy to learn interface without compromising functionality. In particular, Sentaurus Visual is able to load all types of TCAD data generated by Synopsys tools, visualize, analyze, and explore them through a variety of intuitive and easy to use but yet powerful features, like dynamic cuts, probing, plot difference, overlay, and many others, with just a few clicks. Also, it provides a Tcl-based scripting language, mainly for task automation.

Additionally, Sentaurus Visual is built using modern software architectural principles, which gives it the necessary flexibility to permit the rapid development of new features in order to meet user needs.

Description

Sentaurus Visual is a plotting software for visualizing data from simulations and experiments. It enables users to work interactively with data using both a graphical user interface and a scripting language for automated tasks.

Sentaurus Visual allows users to visualize complex simulation results generated by physical simulation tools in 1D, 2D and 3D. Users can visualize data for an initial understanding and analysis, and then modify the plots to gain a new perspective.

Sentaurus Visual can be used to create plots that display fields, geometries, and regions, including results such as p-n junctions and depletion layers. Users can also view I-V curves and doping profiles, and use tools to

zoom, pan, and rotate images, and to extract data using measure and probe tools.

The graphical user interface (GUI) provides direct and easy-to-use functionality, as well as advanced controls for expert users. With the Sentaurus Visual GUI, users can systematically visualize structures as XY, 2D, and 3D plots.

The developers of Sentaurus Visual have been focused to bring important and commonly used features in just few clicks. The following detailed descriptions capture some of the key features and are divided into different groups: first, features available in all the plot dimensions; then, features available only in certain dimensions, grouped by the dimension.

Main features

There are a group of features that are common throughout all the plot dimensions.

Reload

During simulations, calibrations or any other TCAD task, the final results are not always obtained in the first iteration; often several iterations are needed. During these iterations, users need to visualize and analyze the obtained results. Sentaurus Visual provides a reload functionality that covers this need, but not only by reloading the data; it also recalculates any new variable, curve or field that has been created, as well as complete datasets, such as the ones obtained by cutlines and cutplanes.

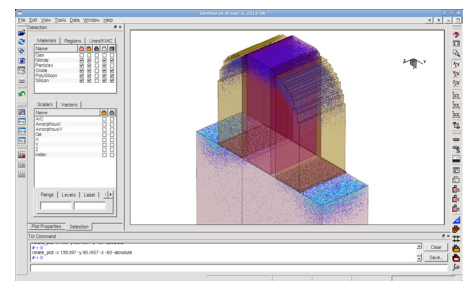


Figure 27: Sentaurus Visual default main interface.



Easy links

Sentaurus Visual provides an easy way to link all the plots of the same dimension. By just selecting all the plots and clicking on the link button, users can link all the properties of the plots, as well as their movement and zoom.

Additionally, a special link functionality is available through a dedicated icon. This feature allows users to connect two or more plot properties such as field selection and range, zoom level, and so on for linked plots. This special link is also available in one button, which opens a dialog with all these options. Finally, automatic linking is an option for those users used to this feature.

Picture exporting

Frequently users need to export the view of their data already processed, for publication in papers or presentations. This can be done by exporting the current view of all the plots in just one image file or in separate files, using the same screen resolution, or by setting a custom resolution. Sentaurus Visual supports multiple file formats. Furthermore, it is possible to export to postscript files, in order to allow scaling without losing quality.

Movie exporting

Movies (or animations) are not only valid to show changes on structures when process parameters are different, when the geometries are modified, or with different operating conditions. They also help to present a structure in motion, as a flight over or through it. This feature brings the possibility to present the analysis results as a GIF format file animation of how the final objective has been obtained. Furthermore, the use of this feature in combination with the dynamic cuts or value blanking features can generate animation that explores and analyzes a structure internally.

Window and panels customization

Sentaurus Visual has a default distribution for all its elements, toolbars and panels (Figure 27), which have been judged to be optimum for from a user efficiency point of view. However, this is not a fixed configuration and users have the option to change it, move and undock all these elements and therefore customize the distribution to meet their needs.

Undo

With every interactive tool, undo cannot be forgotten. Sentaurus Visual implements the undo functionality for the most important actions, as the interactions on the plots, and the configurations of their elements.

Features on XY plots

Sentaurus Visual can be used to display and analyze XY data as curves. Every curve is a sequence of points defined by two arrays of data, x and y coordinates. Sentaurus Visual loads 1D/XY files. They consist of a set of arrays of the same size, where every array is called Variable, and their set is called Dataset. In general, one file contains one dataset, but it could contain more depending on its format. This division of data does not limit the display of curves from different datasets to one plot. The operations to create and modify data are defined on variables and curves, unlike other tools where all operations are defined only on curves.

Managing multiple plots

The possibility to compare multiple curves visually of different magnitudes becomes difficult if the user tries to display all of them in one plot. Sentaurus Visual has the capability to create as many plots as the user wants in order to display each group of curves on different plots at the same time. It allows the display of different groups of I-V curves at once and has flexible frame operations, where one can minimize, maximize, or rearrange plots, without a need to delete them (Figure 28).

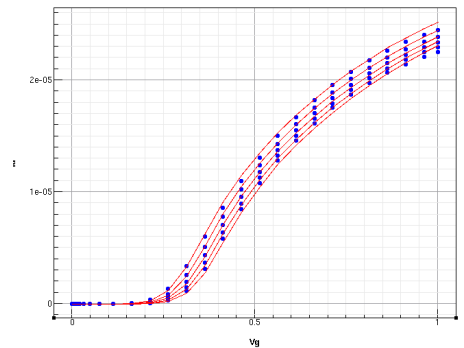
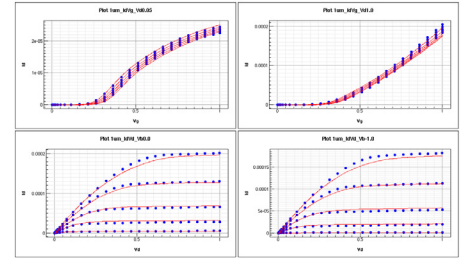


Figure 28: (top) Multiple plots in a grid layout. (bottom) First plot maximized.

Visual probing

Sentaurus Visual provides an easy and friendly way to probe all the curves at once, showing a main guideline of the probe position and, optionally, a secondary guideline for every curve showing the intersection with all of them. Simultaneously, the probed values, for all the curves, are shown in the probe panel.

Easy variables and curves manipulation

Sometimes the data loaded is not precisely what the user wants to analyze or visualize and it may require some transformations, calculations or other kinds of manipulations to obtain the desired result. Sentaurus Visual provides convenient ways to manipulate the loaded data through the calculation of new variables, creation of new curves using the already plotted as base, or transformation of the existing curves by using a complete set of mathematical functions.



Inspect support

Inspect has been and continues to be an important tool for visualization and analysis of 1D/XY data generated by TCAD Sentaurus tools. Sentaurus Visual supports Inspect Tcl command scripts with a special compatibility mode. It allows the user used to Inspect to start working with Sentaurus Visual and be productive from the first launch.

Data exporting

There are multiple sources to obtain new 1D data: generate it by built-in or customized formulas, extract it from cutlines or a mix of both. This new 1D data is usually important and needs to be stored. Sentaurus Visual provides an easy interface to export into ASCII files any kind of 1D data, as selected variables or curves.

Features on 2D/3D plots

Sentaurus Visual has the capability to display and analyze 2D and 3D data. It supports all the file formats, from the standard TCAD Sentaurus TDR file format, to the old DF-ISE file formats.

Dynamic cuts

Cuts, specifically cutlines and cutplanes, are tools to explore the data inside the structures, such as the mesh and fields. Cutplanes help to analyze and visualize internal planes of the structure and the cutlines are used to extract XY data from 2D and 3D data. These cuts could be axis aligned and non-axis aligned.

Sentaurus Visual offers not only the possibility to create these cuts in just two clicks; it makes the original and resulting data dynamically connected (Figure 29). This means that after the cut is created, the user is able to interact with the cut in the original plot, that is, to alter position of the cut, moving it using the mouse or defining a new position with its property panel, and obtain an updated cut plot instantly, without the need to create a new cut. This allows the user to inspect the changes visually with the simple movement of the mouse, all interactively.

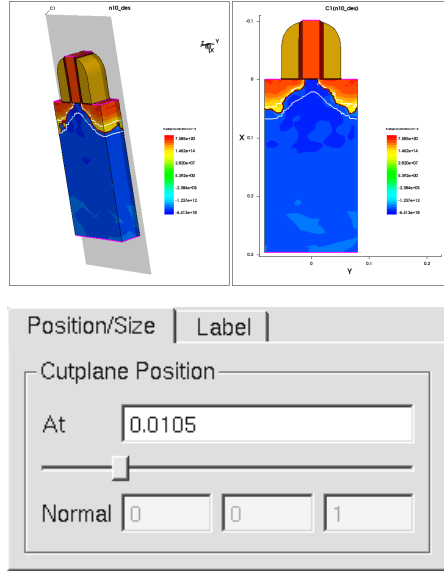


Figure 29: (Top) 3D plot with a cutplane and its resulting 2D cutplane plot. (Bottom) Cutplane properties panel with the option to change its current position.

Easy plot overlay

For TCAD users, comparing all aspects of simulation results are important. Sentaurus Visual provides an easy way to do this in a few clicks: Plot Overlay. This capability is used to compare structures by overlaying boundaries, and to compare mesh and pn-junctions. It is also useful to compare fields by overlaying the contour lines of each structure. These can be used for comparing results of different process conditions and device fabrication sequences and for differences that come from different TCAD input decks, models and parameters, due intentional and unintentional usage (Figure 30).

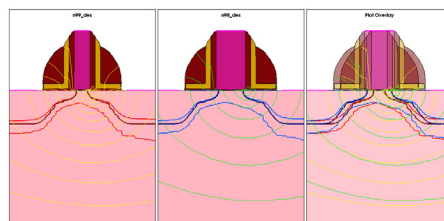


Figure 30: (Left and Center) Two plots to compare. Both plots show the junction line, depletion region and the contour lines of the lattice temperature field, but with different colors. (Right) Resulting plot of overlaying the two plots on the left.

Easy plot difference

Sentaurus Visual provides a capability, called Plot Difference (Figure 31), to calculate the field difference between two different structures, even if they differ slightly in their geometries.

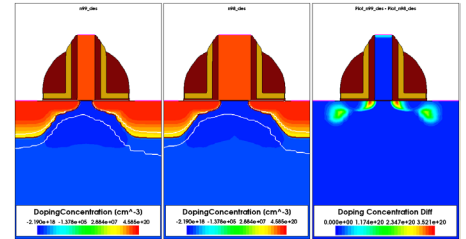


Figure 31: (Left and Center) Two plots to compare. (Right) Resulting comparison plot; the field shown in this plot has been created as the absolute value of the resulting field of the difference of the two plots on the left and center.

3D performance

Some 3D simulations from TCAD Sentaurus tools can generate very large and complex structures. The visualization and manipulation of such structures is critical in terms of performance. Sentaurus Visual offers various options to configure and fine-tune the rendering details, allowing the users to get the best performance possible with their computing environment. This capability provides an easy way to setup a wireframe view of the structure for every movement, making almost any move of the structure smooth. Also it implements a feature called subsampling which enables the rendering of the structure only during interaction. This feature allows users to see the regions and its fields with a lower resolution during its movement.

Tcl commands

Sentaurus Visual provides a Tcl-based scripting language with a full list of commands that gives the user complete control of the tool. Each command has been developed to fulfill the idea of simple, easy and intuitive usage. Furthermore, every action performed by the user is echoed as a



Tcl command (Figure 32). These actions can be saved to be executed in another session. That makes it possible to use the tool for data extraction, as well as data, image and movie exporting, automated tasks or even for live demonstrations. Moreover, the Tcl command panel helps users to remember Sentaurus Visual commands using hints when the user begins typing them.

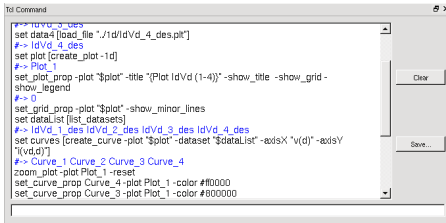


Figure 32: Tcl command panel with a history of commands executed.

Script library

From time to time, new scripts are developed by users to simplify and automate their work. Later, some of these scripts could become common scripts used by other users. Sentaurus Visual allows the storage of Tcl script files as libraries, and their subsequent loading automatically when the tool is invoked. They can be added at user level or even at the installation level to make them available to all the users of the work group.

Integration with other Synopsys TCAD tools

Sentaurus Visual is integrated into the TCAD Sentaurus Workbench; it can be setup as the default visualization tool, load any kind of TCAD Sentaurus file and, as it supports Inspect Tcl commands, it can be used to execute them without major changes.

Summary

Sentaurus Visual is a new generation of TCAD visualization and analysis tool, combining improved ease of use with superior functionality and performance.

References

- [1] B. Yang, K.D. Buddharaju, S.H.G. Teo, J. Fu, N. Singh, G.Q. Lo, and D.L. Kwong. CMOS compatible Gate-All-Around Vertical silicon-nanowire MOSFETs. Solid-State Device Research Conference, 2008. ESSDERC 2008. 38th European, 318-321, 15-19 Sept. 2008.
- [2] N. Burbure, N. G. Rudawski and K.S. Jones, Electrochem. Solid State Letters. 10, H184 (2007)
- [3] Ignacio Martin/Bragado, “[111] local configurations: The main source of silicon defects during solid phase epitaxial regrowth modeled by lattice kinetic Monte Carlo”, Appl. Phys. Lett. 98, 233109 (2011)
- [4] Ignacio Martin-Bragado and Victor Moroz. “Facet formation during solid phase epitaxy regrowth: A lattice kinetic Monte Carlo model”. Appl. Phys. Lett 95, 123123 (2009)
- [5] Ignacio Martin-Bragado and Benoit-Sklenard, “Comprehensive modeling of silicon Solid Phase Epitaxial Regrowth: anisotropy, bi-modal growth, defect formation and interface topology” to be published
- [6] K.L. Saenger et al. “An study of trench-edge defect formation in (001) and (011) silicon recrystallized by solid phase epitaxy”, Journal of Applied Physics 101, 024908 (2007)
- [7] K. Akarvardar et al., “Impact of fin doping and gate stack on FinFET (110) and (100) electron and hole mobilities,” IEEE Electron Device Lett., vol. 33, p. 351 (2012).
- [8] C. Jungemann, S. Keith and B. Meinerzhagen, “Full-band Monte Carlo simulation of a 0.12 μm -Si-PMOSFET with and without a strained SiGe-channel,” International Electron Devices Meeting (IEDM), pp. 897-900, December 1998
- [9] F.M. Buffer and A. Erlebach, “Monte Carlo simulation of the performance dependence on surface and channel orientation in scaled pFinFETs,” European Solid-State Device Research Conference (ESSDERC), Montreux, Switzerland, pp.174-177, September 2006.
- [10] C. Smith et al., “Strain engineering in nanoscale CMOS FinFETs and methods to optimize R^2D ,” Symposium on VLSI Technology, Systems and Applications (VLSI-TSA), Hsinchu, Taiwan, pp. 156-157, April 2010.

- [11] F.M. Buffer et al., “Single-Particle Approach to Self-Consistent Monte Carlo Device Simulation,” IEICE Trans. Electron., vol. E86-C, p. 308 (2003).
- [12] M. Yang et al, “High Performance CMOS Fabricated on Hybrid Substrate with Different Crystal Orientations,” in IEDM Tech. Dig. 2003, 453 (2003).
- [13] R. Pillarisetty et al., “High Mobility Strained Germanium Quantum Well Field Effect Transistor as the P-Channel Device Option for Low Power ($V_{cc} = 0.5\text{ V}$) III-V CMOS Architecture,” in IEDM Tech. Dig. 2010, 231 (2010)
- [14] X.-P. Xu and A. Needleman, “Numerical Simulations of Fast Crack Growth in Brittle Solids,” *Journal of the Mechanics and Physics of Solids*, vol. 42, no. 9, pp. 1397–1434, 1994.
- [15] J. R. Rice, “A Path Independent Integral and the Approximate Analysis of Strain Concentration by Notches and Cracks,” *Journal of Applied Mechanics*, vol. 35, no. 2, pp. 379–386, 1968.
- [16] C. F. Shih, B. Moran, and T. Nakamura, “Energy release rate along a three-dimensional crack front in a thermally stressed body,” *International Journal of Fracture*, vol. 30, no. 2, pp. 79–102, 1986.